


Modeling hydrodynamics, magnetic fields, and synthetic radiographs for high-energy-density plasma flows in shock-shear targets

Cite as: Phys. Plasmas **27**, 012303 (2020); <https://doi.org/10.1063/1.5126149>

Submitted: 30 August 2019 . Accepted: 16 December 2019 . Published Online: 21 January 2020

Yingchao Lu , Shengtai Li , Hui Li , Kirk A. Flippo , Dan Barnak , Andrew Birkel , Brandon Lahmann , Chikang Li, Alexander M. Rasmus , Kwyntero Kelso, Alex Zylstra , Edison Liang, Petros Tzeferacos, and Don Lamb



View Online



Export Citation



CrossMark

ARTICLES YOU MAY BE INTERESTED IN

[Approaching a burning plasma on the NIF](#)

Physics of Plasmas **26**, 052704 (2019); <https://doi.org/10.1063/1.5087256>

[The 2018 James Clerk Maxwell Prize for Plasma Physics](#)

Physics of Plasmas **26**, 080201 (2019); <https://doi.org/10.1063/1.5120399>

[Three-dimensional modeling and hydrodynamic scaling of National Ignition Facility implosions](#)

Physics of Plasmas **26**, 050601 (2019); <https://doi.org/10.1063/1.5091449>



NEW

AVS Quantum Science

A new interdisciplinary home for impactful quantum science research and reviews

Co-Published by



NOW ONLINE

Modeling hydrodynamics, magnetic fields, and synthetic radiographs for high-energy-density plasma flows in shock-shear targets

Cite as: Phys. Plasmas **27**, 012303 (2020); doi: [10.1063/1.5126149](https://doi.org/10.1063/1.5126149)

Submitted: 30 August 2019 · Accepted: 16 December 2019 ·

Published Online: 21 January 2020











View Online



Export Citation



CrossMark

Yingchao Lu,^{1,2,a)}  Shengtai Li,^{1,b)}  Hui Li,^{1,c)}  Kirk A. Flippo,^{3,d)}  Dan Barnak,³  Andrew Birkel,⁴  Brandon Lahmann,⁴  Chikang Li,⁴ Alexander M. Rasmus,⁵  Kwyntero Kelso,⁵ Alex Zylstra,⁶  Edison Liang,² Petros Tzeferacos,⁷ and Don Lamb⁷

AFFILIATIONS

¹Theoretical Division, Los Alamos National Laboratory, Los Alamos, New Mexico 87545, USA

²Department of Physics and Astronomy, Rice University, Houston, Texas 77005, USA

³Laboratory for Laser Energetics, Rochester, New York 14623, USA

⁴Plasma Science and Fusion Center, Massachusetts Institute of Technology, Cambridge, Massachusetts 02139, USA

⁵Physics Division, Los Alamos National Laboratory, Los Alamos, New Mexico 87545, USA

⁶Lawrence Livermore National Laboratory, Livermore, California 94550, USA

⁷Department of Astronomy and Astrophysics, University of Chicago, Chicago, Illinois 60637, USA

^{a)}yclu@lanl.gov

^{b)}slili@lanl.gov

^{c)}hli@lanl.gov

^{d)}kflippo@lanl.gov

ABSTRACT

Three-dimensional FLASH radiation-magnetohydrodynamics (radiation-MHD) modeling is carried out to study the hydrodynamics and magnetic fields in the shock-shear derived platform. Simulations indicate that fields of tens of Tesla can be generated via the Biermann battery effect due to vortices and mix in the counterpropagating shock-induced shear layer. Synthetic proton radiography simulations using MPRAD and synthetic X-ray image simulations using SPECT3D are carried out to predict the observable features in the diagnostics. Quantifying the effects of magnetic fields in inertial confinement fusion and high-energy-density plasmas represents frontier research that has far-reaching implications in basic and applied sciences.

Published under license by AIP Publishing. <https://doi.org/10.1063/1.5126149>

I. INTRODUCTION

When an inertial confinement fusion (ICF) capsule implodes, the material turns into dense plasmas and recent simulations have shown that such plasmas tend to be unstable and turbulence can develop.¹ Even though it is debated whether turbulence is damped by the viscosity in the hot spot, the shocked interfaces as well as the interface between the shell and the hot spot can have very different dynamics and can indeed be unstable.^{2–7} It is believed that turbulence and the associated mixing process can be crucial for understanding ICF.

The Biermann battery effect⁸ is known to generate seed magnetic fields in laser driven plasma flows and has been studied extensively in high-energy-density (HED) laser-driven experiments,^{9–16} but the strength and importance of these fields in the close to or higher than

solid density plasmas such as an ICF implosion are not well known. Three-dimensional extended-magnetohydrodynamic (extended-MHD) simulations of the stagnation phase of ICF including the Biermann battery term,⁸ Nernst term,¹⁷ and anisotropic heat conduction in the magnetic field indicate that self-generated magnetic fields can reach over 10^4 Tesla and can affect the electron heat flow.¹⁸ The simulations with premagnetization for ICF implosions show the significance of Lorentz force and α -particle trapping.¹⁹ In low density laser driven plasmas, the magnetic field can be amplified by turbulence and measured using temporal diagnostics by the B-dot probe²⁰ and spatial diagnostics by proton radiography.²¹ The magnetic frequency spectrum in supersonic plasma turbulence has been measured in a recent experiment²² on the Vulcan laser. However, in those experiments^{20–22}

the magnetic field is not high enough to change the dynamics of the hydrodynamical flow.

In this work, we use the shock-shear platform^{23,24} developed at the Los Alamos National Laboratory (LANL) to quantify the dynamics of magnetic fields in HED plasmas with instabilities and turbulence. The shock compression can achieve a regime where the density is around 1g/cc. The targets with large density can diffuse the proton beam and affect the interpretation of the proton image,²⁵ but the simulations for the synthetic proton image including the stopping power and Coulomb scattering show that the deflection of the proton beam by magnetic fields is still detectable. Further improvements are still needed to make the fields high enough to change the dynamics of the small-scale evolution of vortices like those in a turbulent cascade and affect our understanding of turbulence.

The shock-shear platform,^{23,24} as a platform to isolatedly study the shear-induced instabilities and turbulence production under HED conditions, i.e., pressure larger than 1 Mbar, has been used to investigate the turbulent mixing^{26,27} at material interfaces when subject to multiple shocks and reshocks or high-speed shear.^{23,28} The experiments^{29–33} using the shock-shear platform have been carried out on the OMEGA Laser Facility and National Ignition Facility (NIF). These experiments provide quantitative measurements to assist in validation efforts^{34–36} for mix models, such as the Besnard-Harlow-Rauenzahn (BHR) model.^{37,38} The experimental data and the validation efforts constrain models relevant to integrated HED experiments such as ICF or astrophysical problems. In the shock-shear targets, the Biermann battery ($\nabla n_e \times \nabla T_e$) term⁸ can generate and sustain strong magnetic fields in the vortices due to the misalignment of the density gradient and temperature gradient caused by electron heat conduction. However, the magnetic fields in the shock-shear targets have not been quantified in simulations or experiments.

In this work, we use the radiation-MHD code FLASH^{39,40} to model the evolution of the shock-shear system on OMEGA.⁴¹ The experiment simulated in this paper uses 8 beams each with 500 J energy laser ablation in 1 ns on each side to drive strong adjacent contour-propagating shocks. Kelvin-Helmholtz instability laterally spreads across a thin layer of magnesium, copper, or plastic placed at the interface. The layer is cut with slots to seed the initial density perturbation, which can generate vortices during the evolution of the shock and shear. The temperature of the materials reaches tens of electron-volts, and simulations predict that the Mach number of the postshock flows in the experiment is around 2 on each side of the shear layer. The magnetic field is generated by the Biermann battery term⁸ and dissipated by the resistive term. The X-ray image^{42–44} and the proton radiograph⁹ are predicted and will be compared to the experimental data in a later paper.

This paper is organized as follows. Section II describes simulation methods and the configuration of the target system. In Sec. III, we show the results for hydrodynamics and MHD evolution from FLASH, the synthetic X-ray image using SPECT3D, and the synthetic proton radiography using MPRAD. The conclusions and discussions are given in Sec. IV.

II. SIMULATION METHODS AND CONFIGURATION

The FLASH code^{39,40,45} is used to carry out the detailed physics simulations of our laser experiments to study the dynamics of the shock-shear system. FLASH is a publicly available, multiphysics,

highly scalable parallel, finite-volume Eulerian code and framework whose capabilities include adaptive mesh refinement (AMR), multiple hydrodynamic and MHD solvers,^{46–49} implicit solvers for diffusion using the HYPRE library,⁵⁰ and laser energy deposition. FLASH is capable of using the multi-temperature equation of states and multi-group opacities. To simulate laser-driven High-Energy-Density-Physics (HEDP) experiments, a 3 T treatment, i.e., $T_{\text{rad}} \neq T_{\text{ele}} \neq T_{\text{ion}}$, is usually adopted. The equations which FLASH solves to describe the evolution of the 3 T magnetized plasma are

$$\frac{\partial \rho}{\partial t} + \nabla \cdot (\rho \mathbf{v}) = 0, \quad (1)$$

$$\frac{\partial \rho \mathbf{v}}{\partial t} + \nabla \cdot \left(\rho \mathbf{v} \mathbf{v} - \frac{1}{4\pi} \mathbf{B} \mathbf{B} \right) + \nabla P_{\text{tot}} = 0, \quad (2)$$

$$\begin{aligned} \frac{\partial \rho E_{\text{tot}}}{\partial t} + \nabla \cdot (\mathbf{v}(\rho E_{\text{tot}} + P_{\text{tot}}) - \frac{1}{4\pi} \mathbf{B}(\mathbf{v} \cdot \mathbf{B})) \\ - \frac{1}{4\pi} \nabla \cdot (\mathbf{B} \times (\eta \nabla \times \mathbf{B})) - \frac{1}{4\pi} \nabla \cdot \left(\mathbf{B} \times \frac{c \nabla P_e}{e n_e} \right) = -\nabla \cdot \mathbf{q} + S, \end{aligned} \quad (3)$$

$$\frac{\partial \mathbf{B}}{\partial t} + \nabla \cdot (\mathbf{v} \mathbf{B} - \mathbf{B} \mathbf{v}) = -\nabla \times (\eta_B \nabla \times \mathbf{B}) + \frac{c}{e} \nabla \times \frac{\nabla P_e}{n_e}, \quad (4)$$

where the total pressure is given by $P_{\text{tot}} = P_{\text{ion}} + P_{\text{ele}} + P_{\text{rad}} + (1/8\pi)B^2$, and the total specific energy $E_{\text{tot}} = e_{\text{ion}} + e_{\text{ele}} + e_{\text{rad}} + (1/8\pi)B^2 + \frac{1}{2} \mathbf{v} \cdot \mathbf{v}$. The total heat flux \mathbf{q} is the summation of electron heat flux $\mathbf{q}_e = -\kappa \nabla T_{\text{ele}}$ and radiation flux \mathbf{q}_r , where κ is the Spitzer electron heat conductivity.^{51,52} The flux-limit used for electron thermal conduction is set to be 6% of the free streaming flux $q_{\text{FS}} = n_e k_B T_e \sqrt{k_B T_e / m_e}$. The first term on the R.H.S of Eq. (4) contains the Spitzer magnetic resistivity η_B .^{51,52} The second term on the R.H.S of Eq. (4) is the Biermann battery term, which generates the magnetic field even if there is no seed magnetic field initially. The plasma has zero initial magnetic field in the simulations. Because plasma beta β is much larger than unity, the Hall term is neglectable and not included in the simulations. The Biermann battery term is turned off in the cells adjacent to the shock detected numerically.⁵³ The magnetic field generation near the shock is not calculated because of the convergence problem⁵⁴ for calculating the Biermann battery term on the Eulerian grid. The convergence problem might be resolved on a Lagrangian grid. On the other hand, the shock in this work is highly collisional and with a small thickness compared to the spatial resolution of proton radiography, thus the scale of the magnetic field near the shock is too small to be detectable. The energy equations for the three components are

$$\frac{\partial}{\partial t} (\rho e_{\text{ion}}) + \nabla \cdot (\rho e_{\text{ion}} \mathbf{v}) + P_{\text{ion}} \nabla \cdot \mathbf{v} = \rho \frac{c_{v,\text{ele}}}{\tau_{ei}} (T_{\text{ele}} - T_{\text{ion}}), \quad (5)$$

$$\begin{aligned} \frac{\partial}{\partial t} (\rho e_{\text{ele}}) + \nabla \cdot (\rho e_{\text{ele}} \mathbf{v}) + P_{\text{ele}} \nabla \cdot \mathbf{v} \\ = \rho \frac{c_{v,\text{ele}}}{\tau_{ei}} (T_{\text{ion}} - T_{\text{ele}}) - \nabla \cdot \mathbf{q}_{\text{ele}} + Q_{\text{abs}} - Q_{\text{emis}} + Q_{\text{las}} + Q_{\text{ohm}}, \end{aligned} \quad (6)$$

$$\frac{\partial}{\partial t} (\rho e_{\text{rad}}) + \nabla \cdot (\rho e_{\text{rad}} \mathbf{v}) + P_{\text{rad}} \nabla \cdot \mathbf{v} = \nabla \cdot \mathbf{q}_{\text{rad}} - Q_{\text{abs}} + Q_{\text{emis}}, \quad (7)$$

where $c_{v,ele}$ is the electron specific heat and τ_{ei} is the ion-electron Coulomb collision time. Q_{abs} (absorption) and Q_{emis} (emission) describe the energy transfer between the electron and the radiation, which is modeled using the multigroup flux-limited radiation diffusion. The laser absorption term Q_{las} is computed using ray-tracing in the geometric optics approximation via the inverse-Bremsstrahlung process. Q_{ohm} is the rate of electron energy increase due to Ohmic heating. The auxiliary equations Eqs. (5)–(7) are advanced in time such that the distribution of energy change due to the work and the total shock-heating is based on the pressure ratio of the components, which is a method implemented in FLASH inspired by the radiation-hydrodynamics code RAGE.^{55,56} We use the equation of state and opacity table from PROPACEOS^{57,58} for modeling all the material properties in our target system.

We initialize the FLASH simulation using the geometry and parameters of targets used for OMEGA experiments. The target system is composed of the shock tube, the gold cone for minimizing stray laser light, the foam filling the shock tube, and a plastic cap covering the end of the tube, as shown in Fig. 1. As shown in Fig. 1(c), a window is opened in the middle of the tube and along the path of the proton beam to make the proton beam less diffusive, i.e., less energy lost and scattering. However, the opened window can make the plasma squirt outwardly. We use the foam with density 62 mg/cc, and the foam is divided by a layer with slanted or non-slanted slots, as shown in Figs. 1(e) and 1(f). The end cap is 1 g/cc plastic. The shape of the slots, the material, and the thickness of the layer, and the material of the wall are listed in Table I. Some targets are built with a pepper-pot screen (PPS),⁵⁹ as shown in Fig. 1(b). The PPS is used for a narrow view of the proton deflection signal in proton radiography, reducing the signal contamination from off-center line-of-sight. The 200 μm diameter hole in the middle allows proton beams to go through the central part of the target. Other holes are used as references to register the position of protons. The PPS is a 40 μm thick tantalum foil.

In the initialization, the pressure of all the solid regions is $5 \times 10^3 \text{ bar} (= 5 \times 10^9 \text{ erg/cm}^3)$, and the temperature is calculated self-consistently from the equation of state table. Using the same pressure instead of the same temperature among all the solid regions can prevent one solid region from expanding into another solid region and launching artificial shocks before the high-energy-density conditions are reached. Under HED conditions, the pressure is larger than $10^5 \text{ bar} (= 10^{11} \text{ erg/cm}^3)$; thus, the initial pressure is low enough to have a neglectable effect on the simulations. The vacuum region is initially filled with 10^{-6} g/cc helium to avoid numerical problems in hydrodynamics or MHD solvers. The density is low enough that the effect of helium on the simulations is negligible.

A 3D cartesian grid with $(240 \times 240 \times 464)$ zones is used to resolve a $(1440 \mu\text{m} \times 1440 \mu\text{m} \times 2784 \mu\text{m})$ domain, corresponding to 6 μm per cell width. Using AMR, each zone is adaptively refined to one leaf level, i.e., a resolution of 3 μm or $2^3 = 8$ zones, if the mass fraction of the layer material is larger than 10%. The refinement allows us to efficiently resolve the dynamics near the layer and reduce the computing time spent on the zones far away from the layer. Although we cannot resolve the turbulence dissipation scale with the current computing capability and neither do we use Reynolds-averaging Navier-Stokes (RANS) models such as the BHR model to resolve the small scale dissipation process of the fluid, FLASH is still a suitable tool for designing these experiments because the fabricated layers have low surface roughness.

To model the laser driven energy deposition, we use the spatial and temporal specifications of each of the 16 OMEGA driver beams. Ray tracing by solving the geometric optics and the inverse bremsstrahlung absorption is used. The 16 driver beams are turned on and turned off simultaneously with a 1 ns pulse duration and 8 beams on each side of the target. Each delivers 500 J of energy on a target. The radius of each beam is 283 μm and the intensity distribution we use is Gaussian.

For convention, $t = 0$ is the time for laser turn on. The axis of the shock tube is the z axis. The layer dividing the foam is in the $y - z$ plane, i.e., the plane with $x = 0$ everywhere. The center of the target is at $x = y = z = 0$. The x axis extends through the window.

The primary diagnostic for a temporally and spatially resolved profile of the density and shock propagation in the experiments is the point projection X-ray radiography with a vanadium backlighter at $23\times$ magnification. The backlighter source emits 5180 eV and 5205 eV helium like lines.⁶⁰ The images are recorded on the X-ray framing camera (XRFC).^{42–44} We use SPECT3D^{61,62} to generate the synthetic ray-tracing X-ray image. The line of sight of XRFC is along the y axis, which captures the distortion of the layer.

Proton radiography,⁹ using D^3He (14.7 MeV) protons from fusion, measures magnetic fields. The temporal resolution of the proton radiograph is typically ~ 150 ps and the spatial resolution is typically $\sim 45 \mu\text{m}$. The diffusion of the proton beam caused by Coulomb scattering^{63,64} and stopping power^{65–69} is significant for the targets we use. We use Monte Carlo code MPRAD²⁵ to model the synthetic proton radiography, including the Lorentz force and the effects from Coulomb scattering and stopping power. The proton source stands at $(-0.75 \text{ cm}, 0, 0)$, while the image plate CR39 is located 27 cm from the center on the other side. The line of sight of the proton radiography is perpendicular to the line of sight of the X-ray image. The energy distribution of the proton source we use in the simulation is a Gaussian distribution with $\text{FWHM} = 0.25 \text{ MeV}$ centered at 14.7 MeV.

III. SIMULATION RESULTS

We show the results from FLASH simulations and synthetic radiography to study the evolution and dynamics of the flows in the shock-shear targets in Figs. 2–4. In the synthetic radiographs, the spatial scales of the synthetic radiographs are divided by the magnification to align with the scales on the target system. The target we use in this work is different from previous shock-shear experiments^{28,30,34,35} mainly in two aspects: (1) cut slots in the layer for seeding density perturbation and (2) opened window on the wall for reducing the diffusion of proton beams.

A. Hydrodynamics

We show the evolution of density, electron temperature, and X-ray flux in the first three rows in Figs. 2–4. The gold plugs hold back the shock at one end of each half-cylinder of foam. Two shocks of roughly the same strength in the same material propagate from opposite directions toward the center of the tube. The layer placed in the middle between the two regions collimates the shocked flows and introduces a length scale through its thickness, which will influence the dominant modes of the resulting shear instability. The cut slots in the layer introduce alternating density gradients and cause magnetic field generation by the Biermann battery term, which is discussed in Sec. III C. Because the layer does not fully collimate the shocks, oblique

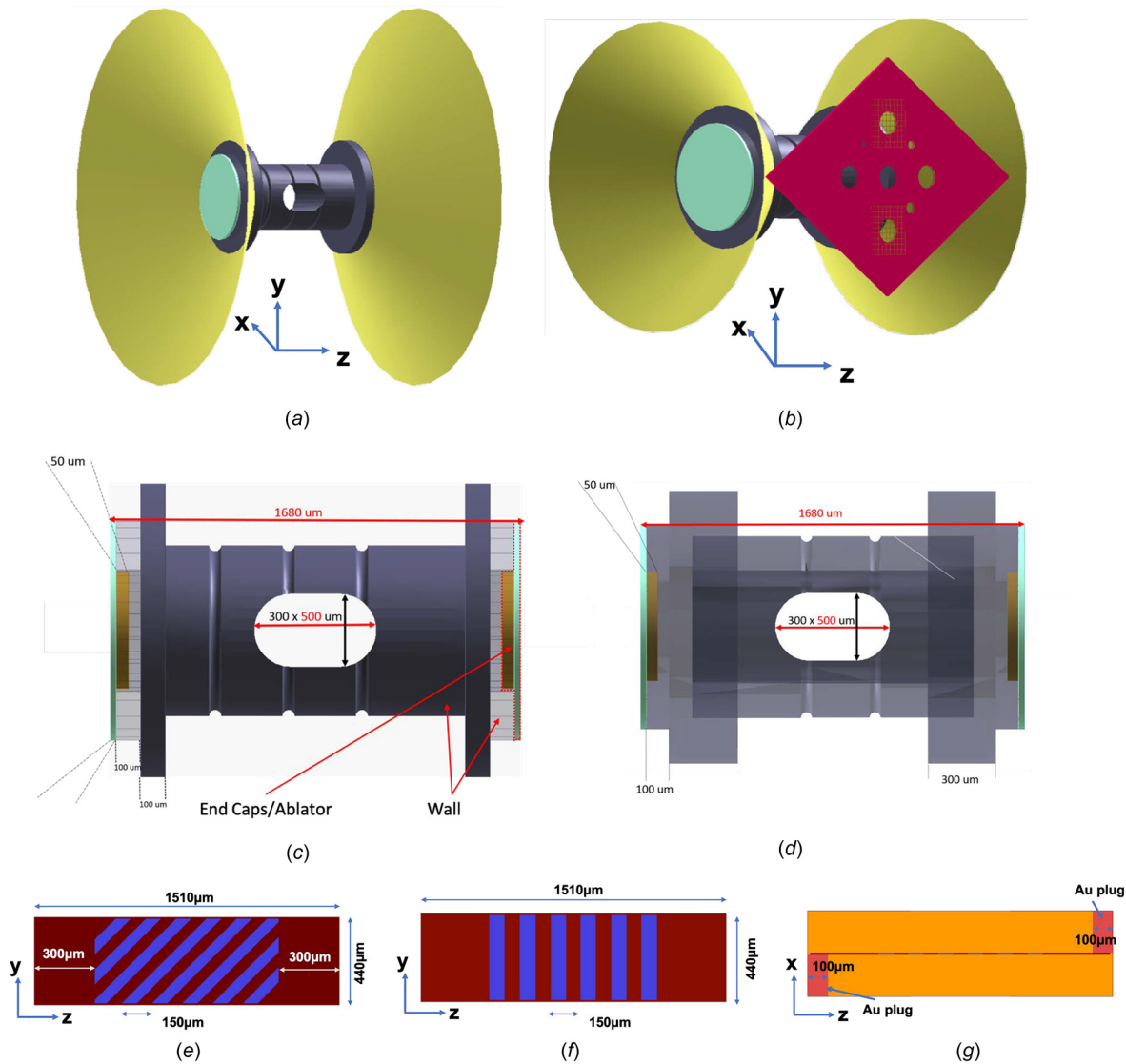


FIG. 1. The experimental setup. The shapes and dimensions of different parts of the target are used to initialize the FLASH simulations. (a) The far-view of the target system, including the shock tube, the gold cone for shielding, and the plastic end cap. The foam and the layer are not shown. The x axis extends through the window. (b) The target with a pepper-pot screen (PPS) for a narrow view proton radiography. The screen has five large holes with $200\ \mu\text{m}$ diameter and four small holes. The screen is at $x = -1.3\ \text{mm}$ plane, attached to the edge of the gold cone. The x axis extends through the window. (c) The dimension of the shock tube, the window, and the end cap. The beryllium shock tube has an oval-shaped window in the middle. The end cap is plastic. The foam and the layer are not in this figure. The inner radius of the tube is $250\ \mu\text{m}$, and the outer radius of the tube is $400\ \mu\text{m}$. (d) Same as (b) but the shock tube is plastic and thicker. The inner radius of the tube is $250\ \mu\text{m}$, and the outer radius of the tube is $400\ \mu\text{m}$. (e) The magnetism layer with 45° slanted slots. The wavelength of the slots is $150\ \mu\text{m}$. (f) The plastic or copper layer with straight slots. The wavelength of the slots is $150\ \mu\text{m}$. (g) A layer divides the low density foam into two half-cylinders to collimate the shock flow. The gold plugs hold back the shock at one end of each half-cylinder of foam.

TABLE I. The parameters and the maximum values of magnetic field and electron temperature for the three different targets/runs we use. T_e and B are calculated by averaging over a $(200\ \mu\text{m})^2$ around the center of the target in the $x - z$ plane. PPS stands for the pepper-pot screen.

Target/run label	Slanted slots	Layer thickness	Layer material	Wall thickness	Wall material	T_e (eV) at 10 ns	B (kGauss) at 10 ns
A	Yes	$15\ \mu\text{m}$	Mg	$100\ \mu\text{m}$	Be	25	158
B	No	$6\ \mu\text{m}$	Cu	$150\ \mu\text{m}$	CH	26	152
C	No	$6\ \mu\text{m}$	CH	$150\ \mu\text{m}$	CH	28	86

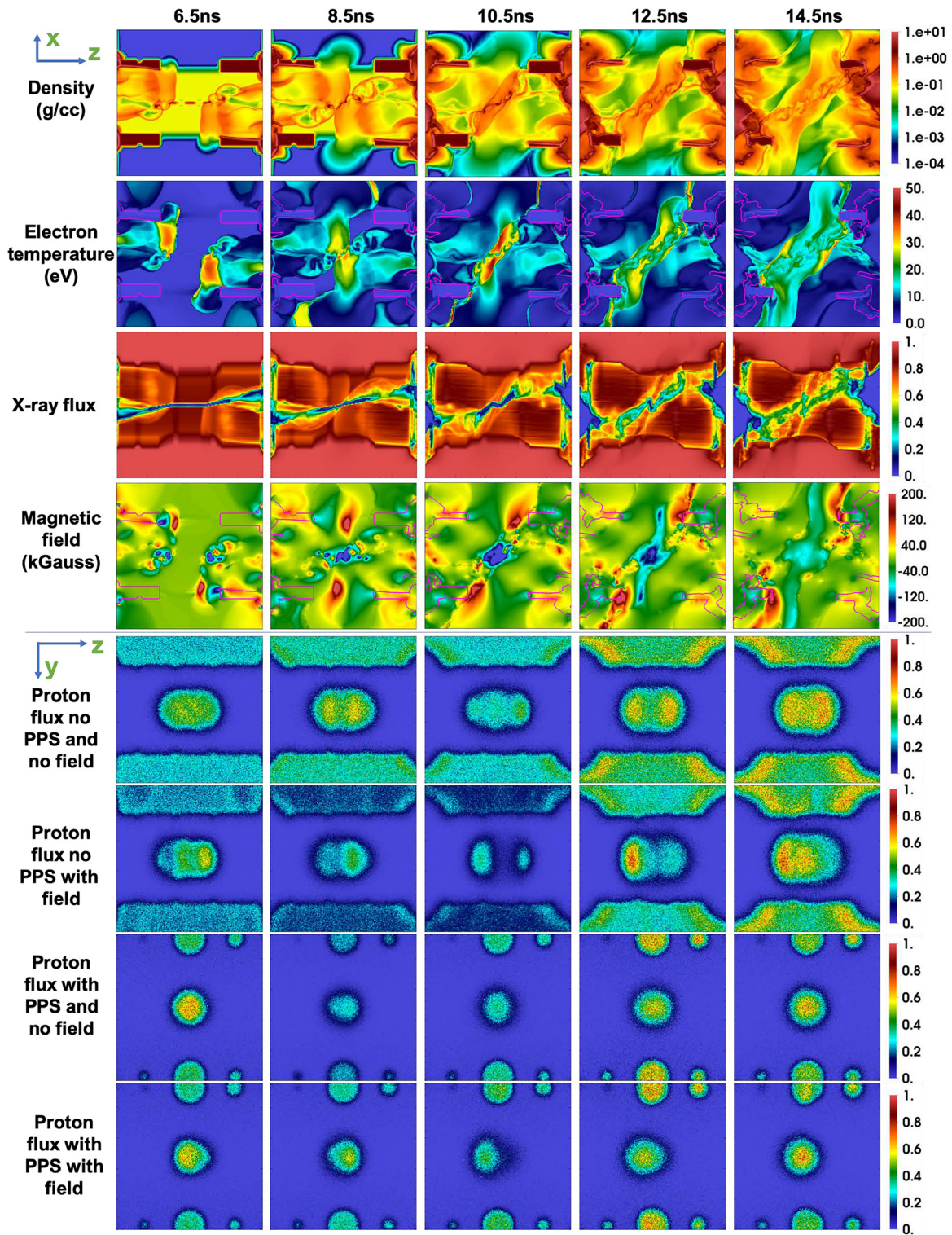


FIG. 2. Spatial distribution of different quantities at different times. The size of all plots is $1200 \mu\text{m} \times 1200 \mu\text{m}$. From first to fourth rows are: density at the $y = 0$ plane, electron temperature at the $y = 0$ plane, X-ray flux normalized by the purely transparent flux, and magnetic field B_y in kGauss at $y = 0$ plane (positive for into the plane). The plots in the second and the fourth rows are overlaid with magenta contours for the density of the wall material equal to 0.5 g/cc . From fifth to the last rows are proton images for four different cases as labeled.

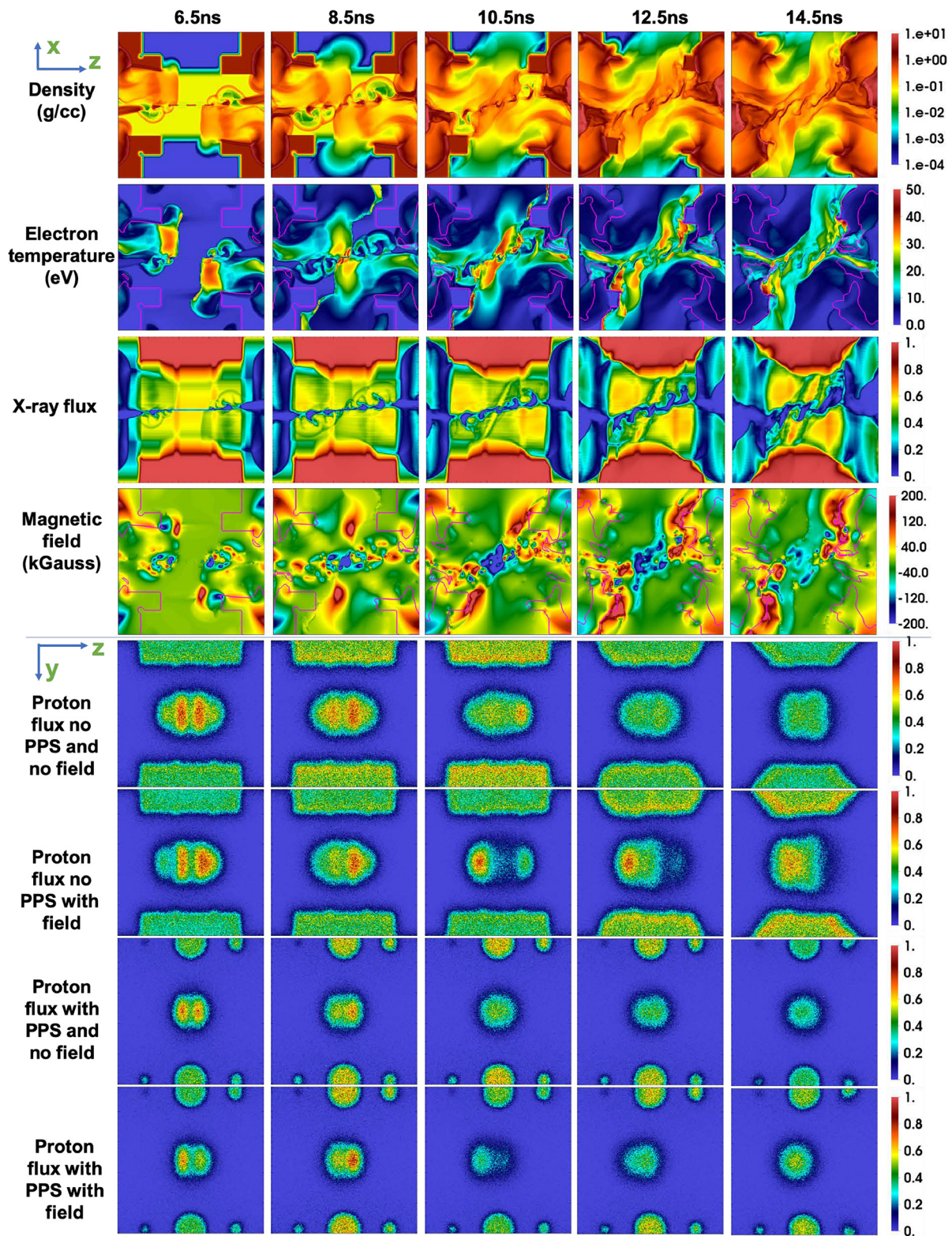


FIG. 3. Same as Fig. 2 but for runB.

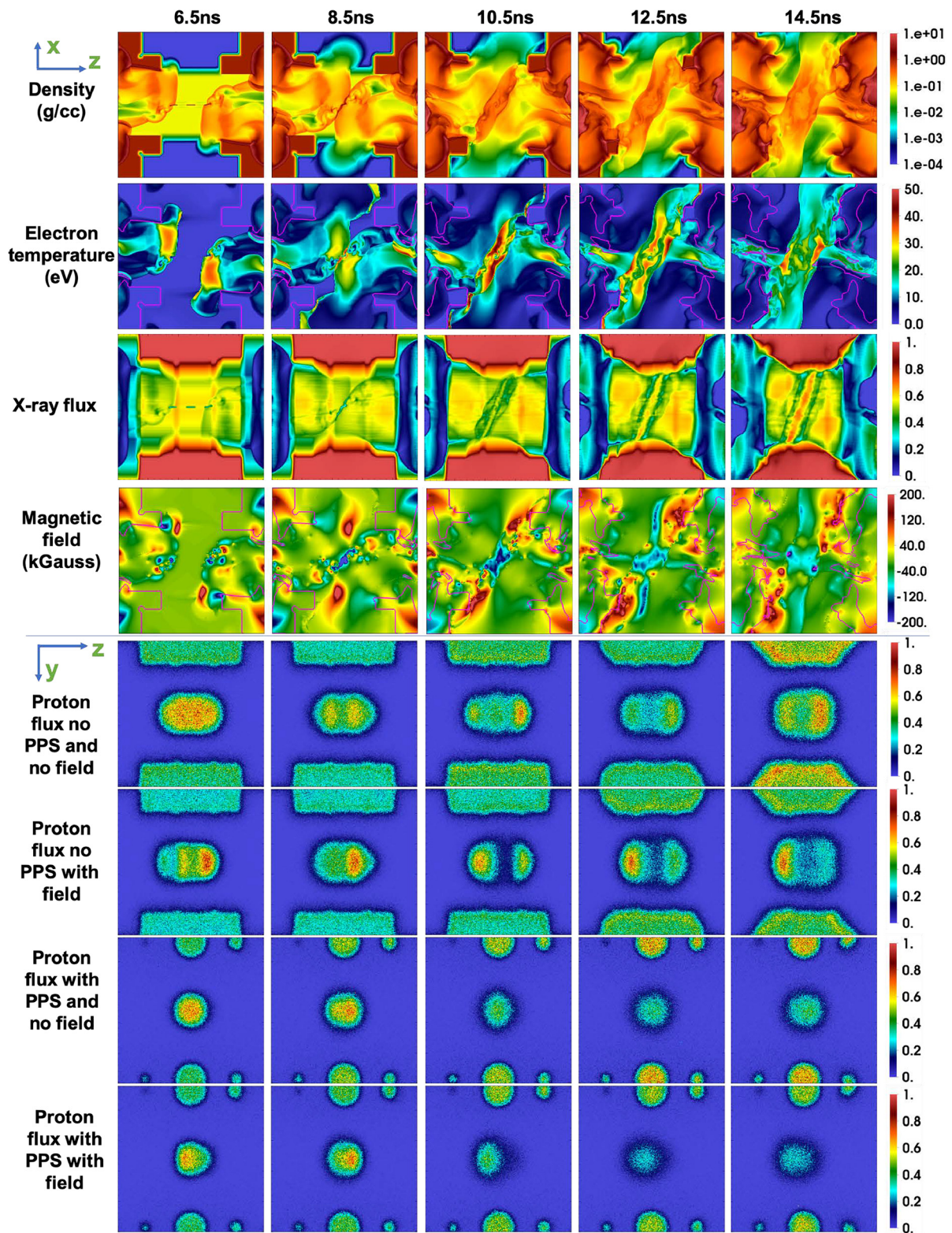


FIG. 4. Same as Fig. 2 but for runC.

shocks are launched into the opposite volumes of the tube. The shock front near the end of the tube travels further transversely. It takes roughly 8.5 ns for the shocks to cross and create the pressure-balanced shear mixing region. The pressure in the two regions is roughly equal and the shocked material is the same on each side of the mixing layer, so that the mixing region does not experience a net translation away from the center of the shock tube. After 8.5 ns, the oblique shock on either end of the tube gradually crosses the primary shock from the other direction. An oblique region of high density is developed by the reverse shock.

The ideally constructed target should be symmetric about a rotation of 180°. However, the different effective laser intensities on two ends of the target due to different laser incident angles cause the two shocks to move at slightly different speeds. The shock from the right side moves slightly faster as shown in the first rows in Figs. 2–4. This asymmetry does not affect the overall picture of the hydrodynamical and magnetic field evolution, but the asymmetry of the density distribution can affect the proton radiography, which is discussed in Sec. III D.

Because of the opened window on the wall, there are plasma plumes traveling outside the window. As shown in Fig. 5, the overall picture of hydrodynamical evolution is still similar to previous shock-shear experiments without a window,^{28,30,34,35} although the plasma plume carries mass and energy away from the tube. At later times, the shock can penetrate through the wall. This results in plumes outside the wall, which can then interact with the plume from the window.

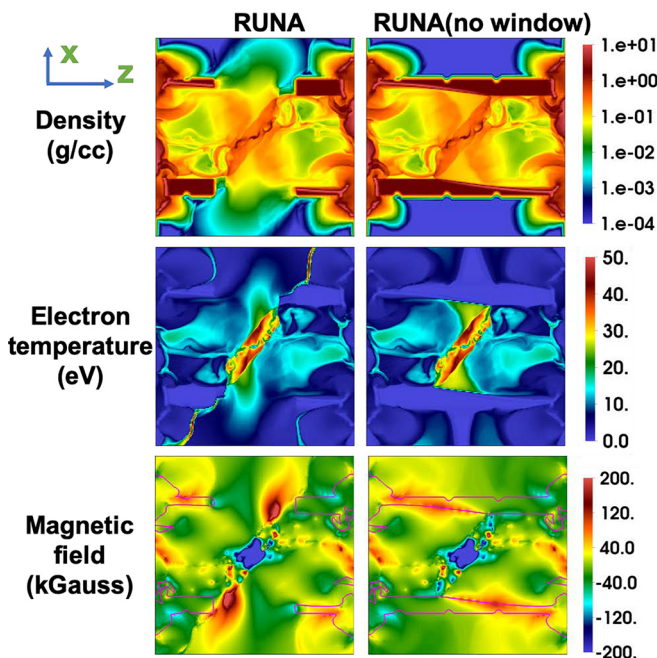


FIG. 5. Spatial distribution of different quantities for runA with or without window at 10 ns. The size of all plots is $1200\ \mu\text{m} \times 1200\ \mu\text{m}$. From first to last rows are density at the $y = 0$ plane, electron temperature at the $y = 0$ plane, and magnetic field B_y in kGauss at $y = 0$ plane (positive for into the plane). The plots in the third row are overlaid with magenta contours for the density of the wall material equal to 0.5 g/cc.

B. X-ray images

The transmitted X-ray flux is shown in the third rows in Figs. 2–4. In the X-ray flux, the location and the shape of the shock front is consistent with the density distribution and can be easily identified. The shocks in the wall can also be seen in the X-ray image. The plume launched from the wall or the window has low density and is not visible in the X-ray flux. The layer has high density and low X-ray transmission, leading to the low flux on the X-ray image. For runA and runB, where the layer material is magnesium and copper, respectively, the contrast of X-ray flux between the layer and the foam is high, while for runC where the layer material is CH, the X-ray contrast is low.

C. Magnetic fields

When the shock from one end of the tube passes, the temperature is high near the center of the half-cylinder as shown in the second rows in Figs. 2–4. A cold region is left behind the shock. The temperature gradient near the layer is perpendicular to the layer and pointing toward the shocked region, due to electron heat conduction. The density gradient is alternating, caused by the cut slots on the layer. Thus, the Biermann battery term generates the alternating magnetic field in the $\pm y$ direction, as shown in Fig. 6(a). However, the cold region left behind the shock has low electron temperature and thus high resistivity. The magnetic fields behind the shock diffuse very quickly. In the end, the only significant field left near the center of the tube is in

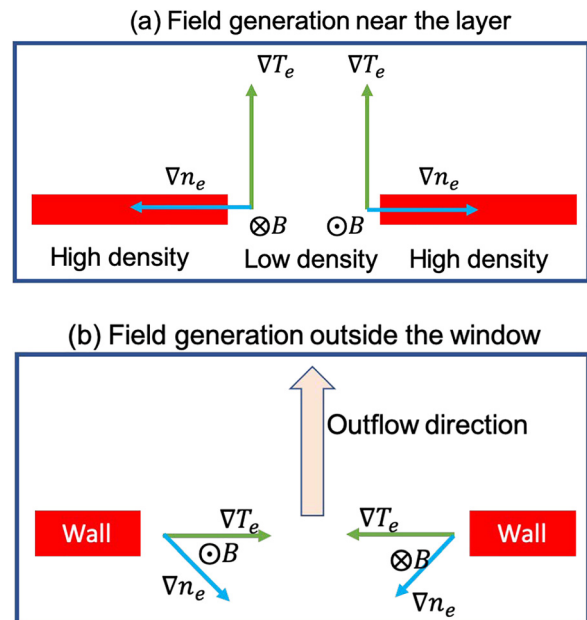


FIG. 6. Schematics of the magnetic field generation by Biermann battery term ($\nabla n_e \times \nabla T_e$). (a) Near the layer, the temperature gradient is perpendicular to the layer due to thermal conduction, the density gradient is alternating and along the layer due to the cut slots on the layer, so that the Biermann generated field is alternating into and out of the plane. (b) Outside the window, the density gradient points to the dense part of the plume, the temperature gradient along the outflow direction is small due to conduction, but the temperature gradient perpendicular to the outflow direction survives due to continuous launching of the plume from the shock tube; thus the field is into the plane on the right side and out of the plane on the left side.

the $-y$ direction, because near the center of the tube, the layer is at high density instead of at a cut slot. On both sides of that high density layer, the field generation is in the $-y$ direction. Two shocks from two ends of the tube cross amplify the magnetic field and create a doubly shocked, high temperature region, which has low resistivity and the field is less diffusive.

The magnetic field in the plume traveling outside the window is generated in a similar way to the magnetic field generated in the ablation plume of a laser interaction with a solid target.^{9,10,12,13} The plume is continuously launched by the flow inside the shock tube and expands in all directions, with the density gradient to point toward the dense part of the plume, as shown in Fig. 6(b). The temperature gradient along the outflow direction is reduced due to electron thermal conduction, but the temperature gradient perpendicular to the outflow direction survives due to continuous launching of the plume from the shock tube. Thus, the magnetic field generated by the Biermann battery term is into the plane on the right side and out of the plane on the left side in Fig. 6(b).

The magnetic field evolution is shown in the fourth rows in Figs. 2–4. In the center of the tube, a field pointing in $-y$ direction dominates. Outside the window, the field pointing in $+y$ direction survives, while the field pointing in $-y$ direction diffuses quickly due to low temperature and high resistivity. The total magnetic flux in the $y=0$ plane is conserved and vanishes. We are interested in the magnetic field near the center of the tube, which can potentially affect the mix. The magnetic field outside the window plays a role in the proton radiography as discussed in Sec. III D, but we are not interested in its dynamical importance because it is far away from the mix region. As shown in Fig. 5, the magnetic field near the center of the tube is similar between the runs with and without the window.

D. Proton radiography

We use the MPRAD code²⁵ to simulate the proton image by taking the output data from 3D FLASH simulations. In the simulations, we use a typical size $45\ \mu\text{m}$ for the proton source. We find that the features of the proton images are most prominent in 14.3 MeV to 14.5 MeV band, i.e., protons losing between 0.2 MeV and 0.4 MeV of kinetic energy. We compare the proton images with/without field, and with/without pepper pot screen (PPS) in the fifth to the last rows in Figs. 2–4. To quantify the asymmetry of the proton image, the averaged horizontal proton position in the blob at the center of the proton image is plotted in Fig. 7. The ideally constructed target should be symmetric about a rotation of 180° and the proton image should also be symmetric in the absence of magnetic field. The asymmetry of the proton image about the vertical axis can be interpreted as the existence of magnetic field.

However, in the no PPS case, i.e., the fifth rows in Figs. 2–4, the blob in the middle of the image can be slightly asymmetric even without magnetic field. This asymmetry is not as large as the asymmetry in the images where there is field but no PPS, i.e., the six rows, which means that the proton deflection by magnetic field causes more asymmetry than by the density asymmetry due to the fact that the shock from the right side in Figs. 2–4, moves slightly faster. This slight difference is caused by the different effective laser intensities on two ends of the target due to different laser incident angles. In the simulations in this work, we do not take into account the unevenness of the foam and the power imbalance on two ends of the tube, which can potentially cause more asymmetry on the proton image than what we show in this work.

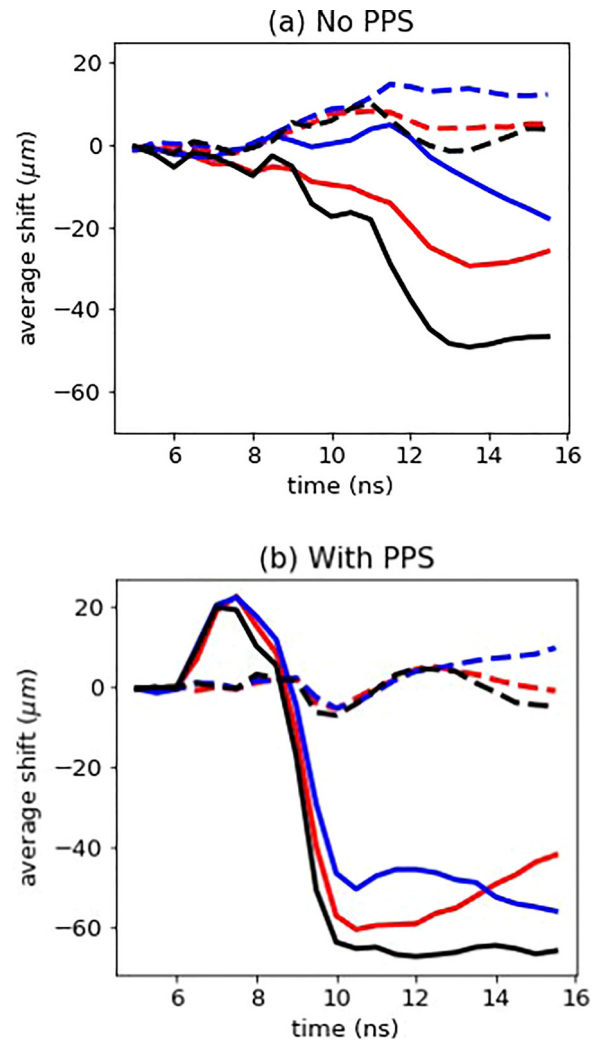


FIG. 7. The evolution of the averaged position of protons in the blob in final energy range 14.3 MeV to 14.5 MeV. The scale is divided by the magnification to align with the scales on the target system. The red curves are for runA, the black curves are for runB, and the blue curves are for runC. The dashed curves are for the MPRAD runs with magnetic field turned off, and the solid curves are for MPRAD runs with magnetic field turned on. (a) is for the no PPS case and (b) is for the with PPS case.

One advantage of using PPS is that the viewing of the surrounding holes is through the regions without the field and the viewing of the hole in the middle is only through the region with magnetic field, so that the net deflection caused by the magnetic field can be determined without another control shot using the same target. With PPS, the asymmetry in the no field case, i.e., the seventh rows in Figs. 2–4, is significantly less than the without field and without the PPS case, i.e., the fifth rows. The PPS is very efficient in reducing the asymmetry of the proton image caused by the intensity imbalance on two ends and the unevenness of the foam. As shown in Fig. 7(b), the asymmetry caused by the proton deflection is significantly larger than that caused by the nonuniform density. The blob has a positive net shift at early time, because of the field pointing in $+y$ direction in the plume outside

the window. At about 8.5 ns, the proton deflection caused by the field pointing in $+y$ direction in the plume outside the window and by the field in near the center of the tube pointing in $-y$ direction cancels, resulting in zero net shift of the blob on the proton image. At a late time $t > 10$ ns, the field pointing in $+y$ direction moves away from the $z=0$ plane, but the field near the center of the tube has no net advection, and the net shift of the blob is negative. The shift value on the image plate divided by the magnification can reach 50–70 μm . The difference between the early time shift and late time shift can reach 70–90 μm . The prediction for the net shift of the blob will be compared to the experimental data to validate the magnetic field model in FLASH.

IV. CONCLUSIONS AND DISCUSSION

We carried out the radiation-MHD simulations and predicted the X-ray and proton images by synthetic radiographs. The hydrodynamical evolution can be measured using XRFC and compared with the simulation results. The predicted proton radiography shows the direction and the amount of the shift of the proton beam going through the window and/or PPS. Although the target can diffuse the proton beam significantly, the evolution of the shift in the synthetic proton radiography is still consistent with the evolution of the magnetic fields in the target system and shows change between early time

and late time. However, the prediction only shows the signal contribution from the mean magnetic fields from different columns along the line of sight. The signal from small scale fields always gets damped by the diffusion of the proton beam. The high energy proton beam accelerated by the Target Normal Sheath Acceleration (TNSA) mechanism using the OMEGA EP beam experiences less diffusion through the target.⁷⁰ The Coulomb scattering angle is roughly proportional to E_p^{-2} , where E_p is the kinetic energy of the proton.^{25,63,64}

The simulation shows that the design we use can achieve a regime with high plasma beta β . The Hall parameter χ , defined by the ratio of electron gyrofrequency to electron collision frequency, is small. The Reynolds number Re is high enough to ensure turbulence, and the magnetic Reynolds number Rm is around 50. Under the condition with these dimensionless parameters, the magnetic field remains dynamically unimportant. The magnetic energy density from Table II is 10^9 erg/s, which is only 0.3% of the turbulent kinetic energy reported in the simulation in Ref. 35 for a previous mix modeling for shock-shear targets under similar conditions to this work. Thus, the magnetic field is also negligible for mix modeling in the shock-shear targets. It is desirable to optimize the measurable magnetic fields and improve the dynamical importance of the magnetic fields.

The Biermann battery generated magnetic field is roughly $ck_B T_e / eLu$ by balancing the Biermann battery term with the

TABLE II. Simulated plasma properties for runA. All quantities are in cgs units except temperature, which is expressed in eV. The length scale, L is approximately the diameter of the tube ($\approx 500 \mu\text{m}$). The n_e , ρ , T_e , and T_i are calculated by averaging over a $(200^2 \mu\text{m})^2$ square around the center of the target in the $x-z$ plane, at $t = 10$ ns. The flow speed is $u = 7 \times 10^6$ cm/s for each counter propagating flow.

Plasma property	Formula	Value at $r = 0$
Electron density $n_e(\text{cm}^{-3})$...	5.6×10^{22}
Mass density $\rho(\text{g}/\text{cm}^3)$...	0.36
Electron temperature $T_e(\text{eV})$...	25
Ion temperature $T_i(\text{eV})$...	25
Magnetic field B (gauss)	...	1.6×10^5
Average ionization Z	...	1.9
Average atomic weight A	...	7.3
Flow speed $u(\text{cm}/\text{s})$...	7×10^6
Sound speed $c_s(\text{cm}/\text{s})$	$\frac{9.8 \times 10^5 [ZT_e + 1.67T_i]^{1/2}}{A^{1/2}}$	3.4×10^6
Mach number M	$\frac{u}{c_s}$	2
Coulomb logarithm $\ln \Lambda$	$\min(23.5 + \ln(T_e^{1.5}/n_e^{0.5}/Z), 25.3 + \ln(T_e/n_e^{0.5}))$	1.4
Hall parameter χ	$6.1 \times 10^{12} \frac{T_e^{3/2} B}{Z n_e \ln \Lambda}$	8×10^{-4}
Plasma β	$\frac{2.4 \times 10^{-12} n_e (T_e + T_i/Z)}{B^2/(8\pi)}$	5×10^3
Péclet number Pe	$uL / \left(\frac{\kappa_e}{\frac{3}{2} n_e k_B} \right) \left(\frac{\kappa_e}{\frac{3}{2} n_e k_B} = 5.5 \times 10^{21} \frac{T_e^{5/2}}{n_e (3.3 + Z) \ln \Lambda} \right)$	8.3×10^3
Magnetic Reynolds number Rm	$uL/\eta \left(\eta = 8.2 \times 10^5 \frac{(0.33Z + 0.18) \ln \Lambda}{T_e^{3/2}} \right)$	47
Reynolds number Re	$uL/\nu \left(\nu = 1.9 \times 10^{19} \frac{T_i^{5/2}}{A^{1/2} Z^3 n_e \ln \Lambda} \right)$	8.6×10^6

advection term. The plasma beta β is then proportional to $n_e T_e / (T_e / Lu)^2 \propto n_e u^2 / L^2 T_e$. If we keep the size of the target and the laser power, $n_e u^2$ and L are roughly constants, and then $\beta \propto 1/T_e$. Thus, increasing T_e can reduce β and make the Lorentz force more important. The Hall parameter⁵² χ is proportional to $T_e^{3/2} / n_e$ and the magnetic Reynolds number Rm is proportional to $T_e^{3/2}$. Both χ and Rm increase with temperature. For low Rm and low magnetic Prandtl number Pr_m , i.e., $Pr_m = Rm/Re \ll 1$, the power spectrum of the kinetic energy $E(k)$ and the power spectrum of the magnetic energy $M(k)$ are related by $M(k) \propto k^{-2} E(k)$, and $M(k)$ is always softer than $E(k)$, and the magnetic field remains dynamically unimportant even in small scales.^{20,71,72} High Rm is favorable for the amplification of magnetic fields and a hard power law for the magnetic energy spectrum.^{21,71,73} One way to achieve a higher temperature is to lower the density of the foam. However, making a low density foam in the target is challenging for target fabrication. It causes the unevenness in the foam, leads to the unevenness of the proton image, and makes it difficult to interpret the experimental data from proton radiography. In a low density foam, the flow may move too fast so that the time window for diagnostics is narrow.

Some experiments⁷⁴ and theories^{75,76} show that around 10 eV, the value of electrical resistivity [electrical resistivity η is related to magnetic resistivity η_B by $\eta_B = (c^2/4\pi)\eta$] is different from the Spitzer resistivity. However, the electrical resistivity with temperature and density dependency under the condition of our experimental design is not well constrained. If the modeling in this work is correct in terms of electrical resistivity, then this would indicate that the magnetic field may not be dynamically important. However, if the electrical resistivity is significantly lower than the Spitzer resistivity that we use in this work, then the simulations in this work underestimates the magnetic fields, and the mix model could potentially cover up the magnetic field effects by the choice of the initial input conditions for the model. Future experiments executed at higher temperatures can potentially make magnetic fields start to play a more important role. In the future development of the simulations, the implementation of the implicit method for the magnetic diffusion equation is desirable for the case of large resistivity where a fully explicit method requires a small time step.

ACKNOWLEDGMENTS

The research presented in this paper was supported by the Laboratory Directed Research and Development (LDRD) Program of the Los Alamos National Laboratory (LANL) under Contract No. 20180040DR. The simulations were performed with LANL Institutional Computing, which is supported by the U.S. Department of Energy National Nuclear Security Administration under Contract No. 89233218CNA000001, and with the Extreme Science and Engineering Discovery Environment (XSEDE), which is supported by the National Science Foundation (NSF) under Grant No. ACI-1548562.

REFERENCES

- C. R. Weber, D. S. Clark, A. W. Cook, L. E. Busby, and H. F. Robey, *Phys. Rev. E* **89**, 053106 (2014).
- D. S. Clark, M. M. Marinak, C. R. Weber, D. C. Eder, S. W. Haan, B. A. Hammel, D. E. Hinkel, O. S. Jones, J. L. Milovich, P. K. Patel, H. F. Robey, J. D. Salmonson, S. M. Sepke, and C. A. Thomas, *Phys. Plasmas* **22**, 022703 (2015).
- B. M. Haines, E. L. Vold, K. Molvig, C. Aldrich, and R. Rauenzahn, *Phys. Plasmas* **21**, 092306 (2014).
- B. M. Haines, G. P. Grim, J. R. Fincke, R. C. Shah, C. J. Forrest, K. Silverstein, F. J. Marshall, M. Boswell, M. M. Fowler, R. A. Gore, A. C. Hayes-Sterbenz, G. Jungman, A. Klein, R. S. Rundberg, M. J. Steinkamp, and J. B. Wilhelmly, *Phys. Plasmas* **23**, 072709 (2016).
- T. Haxhimali, R. E. Rudd, W. H. Cabot, and F. R. Graziani, *Phys. Rev. E* **92**, 053110 (2015).
- E. L. Vold, A. S. Joglekar, M. I. Ortega, R. Moll, D. Fenn, and K. Molvig, *Phys. Plasmas* **22**, 112708 (2015).
- E. Vold, A. Joglekar, M. Ortega, R. Moll, D. Fenn, and K. Molvig, *J. Phys.: Conf. Ser.* **717**, 012056 (2016).
- L. Biermann, *Z. Naturforsch. Teil A* **5**, 65 (1950).
- C. K. Li, F. H. Séguin, J. A. Frenje, J. R. Rygg, R. D. Petrasso, R. P. J. Town, P. A. Amendt, S. P. Hatchett, O. L. Landen, A. J. Mackinnon, P. K. Patel, V. A. Smalyuk, T. C. Sangster, and J. P. Knauer, *Phys. Rev. Lett.* **97**, 135003 (2006).
- C. A. Cecchetti, M. Borghesi, J. Fuchs, G. Schurtz, S. Kar, A. Macchi, L. Romagnani, P. A. Wilson, P. Antici, R. Jung, J. Osterholtz, C. A. Pipahl, O. Willi, A. Schiavi, M. Notley, and D. Neely, *Phys. Plasmas* **16**, 043102 (2009).
- L. Gao, E. Liang, Y. Lu, R. K. Follet, H. Sio, P. Tzeferacos, D. H. Froula, A. Birkel, C. K. Li, D. Lamb, R. Petrasso, W. Fu, M. Wei, and H. Ji, *Astrophys. J.* **873**, L11 (2019).
- C. K. Li, F. H. Séguin, J. A. Frenje, J. R. Rygg, R. D. Petrasso, R. P. J. Town, P. A. Amendt, S. P. Hatchett, O. L. Landen, A. J. Mackinnon, P. K. Patel, M. Tabak, J. P. Knauer, T. C. Sangster, and V. A. Smalyuk, *Phys. Rev. Lett.* **99**, 015001 (2007).
- C. K. Li, F. H. Séguin, J. A. Frenje, M. Manuel, D. Casey, N. Sinenian, R. D. Petrasso, P. A. Amendt, O. L. Landen, J. R. Rygg, R. P. J. Town, R. Betti, J. Delettrez, J. P. Knauer, F. Marshall, D. D. Meyerhofer, T. C. Sangster, D. Shvarts, V. A. Smalyuk, J. M. Soares, C. A. Back, J. D. Kilkenny, and A. Nikroo, *Phys. Plasmas* **16**, 056304 (2009).
- C. K. Li, D. D. Ryutov, S. X. Hu, M. J. Rosenberg, A. B. Zylstra, F. H. Séguin, J. A. Frenje, D. T. Casey, M. G. Johnson, M. J.-E. Manuel, H. G. Rinderknecht, R. D. Petrasso, P. A. Amendt, H. S. Park, B. A. Remington, S. C. Wilks, R. Betti, D. H. Froula, J. P. Knauer, D. D. Meyerhofer, R. P. Drake, C. C. Kuranz, R. Young, and M. Koenig, *Phys. Rev. Lett.* **111**, 235003 (2013).
- R. D. Petrasso, C. K. Li, F. H. Séguin, J. R. Rygg, J. A. Frenje, R. Betti, J. P. Knauer, D. D. Meyerhofer, P. A. Amendt, D. H. Froula, O. L. Landen, P. K. Patel, J. S. Ross, and R. P. J. Town, *Phys. Rev. Lett.* **103**, 085001 (2009).
- G. Gregori, A. Ravasio, C. D. Murphy, K. Schaer, A. Baird, A. R. Bell, A. Benuzzi-Mounaix, R. Bingham, C. Constantin, R. P. Drake, M. Edwards, E. T. Everson, C. D. Gregory, Y. Kuramitsu, W. Lau, J. Mithen, C. Niemann, H.-S. Park, B. A. Remington, B. Reville, A. P. L. Robinson, D. D. Ryutov, Y. Sakawa, S. Yang, N. C. Woolsey, M. Koenig, and F. Miniati, *Nature* **481**, 480 (2012).
- A. Nishiguchi, T. Yabe, M. G. Haines, M. Psimopoulos, and H. Takewaki, *Phys. Rev. Lett.* **53**, 262 (1984).
- C. Walsh, J. Chittenden, K. McGlinchey, N. Niasse, and B. Appelbe, *Phys. Rev. Lett.* **118**, 155001 (2017).
- C. A. Walsh, K. McGlinchey, J. K. Tong, B. D. Appelbe, A. Crilly, M. F. Zhang, and J. P. Chittenden, *Phys. Plasmas* **26**, 022701 (2019).
- J. Meinecke, H. W. Doyle, F. Miniati, A. R. Bell, R. Bingham, R. Crowston, R. P. Drake, M. Fatenejad, M. Koenig, Y. Kuramitsu, C. C. Kuranz, D. Q. Lamb, D. Lee, M. J. MacDonald, C. D. Murphy, H.-S. Park, A. Pelka, A. Ravasio, Y. Sakawa, A. A. Schekochihin, A. Scopatz, P. Tzeferacos, W. C. Wan, N. C. Woolsey, R. Yurchak, B. Reville, and G. Gregori, *Nat. Phys.* **10**, 520 (2014).
- P. Tzeferacos, A. Rigby, A. F. A. Bott, A. R. Bell, R. Bingham, A. Casner, F. Cattaneo, E. M. Churazov, J. Emig, F. Fiuza, C. B. Forest, J. Foster, C. Graziani, J. Katz, M. Koenig, C.-K. Li, J. Meinecke, R. Petrasso, H.-S. Park, B. A. Remington, J. S. Ross, D. Ryu, D. Ryutov, T. G. White, B. Reville, F. Miniati, A. A. Schekochihin, D. Q. Lamb, D. H. Froula, and G. Gregori, *Nat. Commun.* **9**, 591 (2018).
- T. G. White, M. T. Oliver, P. Mabey, M. Kühn-Kauffeldt, A. F. A. Bott, L. N. K. Döhl, A. R. Bell, R. Bingham, R. Clarke, J. Foster, G. Giacinti, P. Graham, R. Heathcote, M. Koenig, Y. Kuramitsu, D. Q. Lamb, J. Meinecke, T. Michel, F. Miniati, M. Notley, B. Reville, D. Ryu, S. Sarkar, Y. Sakawa, M. P. Selwood, J. Squire, R. H. H. Scott, P. Tzeferacos, N. Woolsey, A. A. Schekochihin, and G. Gregori, *Nat. Commun.* **10**, 1758 (2019).

- ²³L. Welser-Sherrill, J. Fincke, F. Doss, E. Loomis, K. Flippo, D. Offermann, P. Keiter, B. Haines, and F. Grinstein, *High Energy Density Phys.* **9**, 496 (2013).
- ²⁴D. Capelli, D. W. Schmidt, T. Cardenas, G. Rivera, R. B. Randolph, F. Fierro, E. C. Merritt, K. A. Flippo, F. W. Doss, and J. L. Kline, *Fusion Sci. Technol.* **70**, 316 (2016).
- ²⁵Y. Lu, H. Li, K. A. Flippo, K. Kelso, A. Liao, S. Li, and E. Liang, *Rev. Sci. Instrum.* **90**, 123503 (2019).
- ²⁶K. A. Flippo, F. W. Doss, B. Devolder, J. R. Fincke, E. N. Loomis, J. L. Kline, and L. Welser-Sherrill, *J. Phys.: Conf. Ser.* **688**, 012018 (2016).
- ²⁷K. Flippo, F. Doss, J. Kline, E. Merritt, D. Capelli, T. Cardenas, B. DeVolder, F. Fierro, C. Huntington, L. Kot, E. Loomis, S. MacLaren, T. Murphy, S. Nagel, T. Perry, R. Randolph, G. Rivera, and D. Schmidt, *Phys. Rev. Lett.* **117**, 225001 (2016).
- ²⁸E. Merritt, F. Doss, C. D. Stefano, K. Flippo, A. Rasmus, and D. Schmidt, *High Energy Density Phys.* **23**, 90 (2017).
- ²⁹F. W. Doss, J. L. Kline, K. A. Flippo, T. S. Perry, B. G. DeVolder, I. Tregillis, E. N. Loomis, E. C. Merritt, T. J. Murphy, L. Welser-Sherrill, and J. R. Fincke, *Phys. Plasmas* **22**, 056303 (2015).
- ³⁰E. C. Merritt, F. W. Doss, E. N. Loomis, K. A. Flippo, and J. L. Kline, *Phys. Plasmas* **22**, 062306 (2015).
- ³¹K. A. Flippo, F. W. Doss, E. C. Merritt, B. G. DeVolder, C. A. D. Stefano, P. A. Bradley, D. Capelli, T. Cardenas, T. R. Desjardins, F. Fierro, C. M. Huntington, J. L. Kline, L. Kot, S. Kurien, E. N. Loomis, S. A. MacLaren, T. J. Murphy, S. R. Nagel, T. S. Perry, R. B. Randolph, A. Rasmus, and D. W. Schmidt, *Phys. Plasmas* **25**, 056315 (2018).
- ³²F. W. Doss, K. A. Flippo, D. Capelli, T. Cardenas, B. DeVolder, J. Kline, L. Kot, S. Kurien, E. Loomis, E. C. Merritt, T. Perry, D. Schmidt, and C. D. Stefano, *J. Phys.: Conf. Ser.* **717**, 012059 (2016).
- ³³F. W. Doss, K. A. Flippo, and E. C. Merritt, *Phys. Rev. E* **94**, 023101 (2016).
- ³⁴F. W. Doss, J. R. Fincke, E. N. Loomis, L. Welser-Sherrill, and K. A. Flippo, *Phys. Plasmas* **20**, 122704 (2013).
- ³⁵F. W. Doss, E. N. Loomis, L. Welser-Sherrill, J. R. Fincke, K. A. Flippo, and P. A. Keiter, *Phys. Plasmas* **20**, 012707 (2013).
- ³⁶P. Wang, Y. Zhou, S. A. MacLaren, C. M. Huntington, K. S. Raman, F. W. Doss, and K. A. Flippo, *Phys. Plasmas* **22**, 112701 (2015).
- ³⁷A. Banerjee, R. A. Gore, and M. J. Andrews, *Phys. Rev. E* **82**, 046309 (2010).
- ³⁸B. M. Haines, F. F. Grinstein, and J. D. Schwarzkopf, *J. Turbul.* **14**, 46 (2013).
- ³⁹B. Fryxell, K. Olson, P. Ricker, F. X. Timmes, M. Zingale, D. Q. Lamb, P. MacNeice, R. Rosner, J. W. Truran, and H. Tufo, *Astrophys. J. Suppl. Ser.* **131**, 273 (2000).
- ⁴⁰A. Dubey, K. Antypas, M. K. Ganapathy, L. B. Reid, K. Riley, D. Sheeler, A. Siegel, and K. Weide, *Parallel Comput.* **35**, 512 (2009).
- ⁴¹T. Boehly, D. Brown, R. Craxton, R. Keck, J. Knauer, J. Kelly, T. Kessler, S. Kumpan, S. Loucks, S. Letzring, F. Marshall, R. McCrory, S. Morse, W. Seka, J. Soures, and C. Verdon, *Opt. Commun.* **133**, 495 (1997).
- ⁴²L. R. Benedetti, P. M. Bell, D. K. Bradley, C. G. Brown, S. M. Glenn, R. Heeter, J. P. Holder, N. Izumi, S. F. Khan, G. Lacaille, N. Simanovskaia, V. A. Smalyuk, and R. Thomas, *Rev. Sci. Instrum.* **83**, 10E135 (2012).
- ⁴³D. K. Bradley, P. M. Bell, J. D. Kilkeny, R. Hanks, O. Landen, P. A. Jaanimagi, P. W. McKenty, and C. P. Verdon, *Rev. Sci. Instrum.* **63**, 4813 (1992).
- ⁴⁴D. K. Bradley, P. M. Bell, O. L. Landen, J. D. Kilkeny, and J. Oertel, *Rev. Sci. Instrum.* **66**, 716 (1995).
- ⁴⁵See <https://flash.uchicago.edu/> for “FLASH4.”
- ⁴⁶P. Roe, *J. Comput. Phys.* **43**, 357 (1981).
- ⁴⁷S. Li, *J. Comput. Phys.* **203**, 344 (2005).
- ⁴⁸T. Miyoshi and K. Kusano, *J. Comput. Phys.* **208**, 315 (2005).
- ⁴⁹E. F. Toro, *Riemann Solvers and Numerical Methods for Fluid Dynamics* (Springer Berlin Heidelberg, 2009).
- ⁵⁰R. D. Falgout and U. M. Yang, in *Lecture Notes in Computer Science* (Springer Berlin Heidelberg, 2002) pp. 632–641.
- ⁵¹L. Spitzer and R. J. Seeger, *Am. J. Phys.* **31**, 890 (1963).
- ⁵²S. I. Braginskii, *Rev. Plasma Phys.* **1**, 205 (1965).
- ⁵³D. S. Balsara and D. S. Spicer, *J. Comput. Phys.* **149**, 270 (1999).
- ⁵⁴C. Graziani, P. Tzeferacos, D. Lee, D. Q. Lamb, K. Weide, M. Fatenejad, and J. Miller, *Astrophys. J.* **802**, 43 (2015).
- ⁵⁵M. Gittings, R. Weaver, M. Clover, T. Betlach, N. Byrne, R. Coker, E. Dendy, R. Hueckstaedt, K. New, W. R. Oakes, D. Ranta, and R. Stefan, *Comput. Sci. Discovery* **1**, 015005 (2008).
- ⁵⁶B. M. Haines, C. H. Aldrich, J. M. Campbell, R. M. Rauenzahn, and C. A. Wingate, *Phys. Plasmas* **24**, 052701 (2017).
- ⁵⁷J. MacFarlane, I. Golovkin, and P. Woodruff, *J. Quant. Spectrosc. Radiat. Transfer* **99**, 381 (2006).
- ⁵⁸See <http://www.prism-cs.com/Software/Propaceos/overview.html> for “Prism Computational Sciences PrOpacEOS Overview.”
- ⁵⁹E. Brunetti, R. P. Shanks, G. G. Manahan, M. R. Islam, B. Ersfeld, M. P. Anania, S. Cipiccia, R. C. Issac, G. Raj, G. Vieux, G. H. Welsh, S. M. Wiggins, and D. A. Jaroszynski, *Phys. Rev. Lett.* **105**, 215007 (2010).
- ⁶⁰A. C. Thompson, D. T. Attwood, E. M. Gullikson, M. R. Howells, J. B. Kortright, A. L. Robinson, and J. H. Underwood, *X-Ray Data Booklet* (Lawrence Berkeley National Laboratory, University of California Berkeley, CA, 2001), Vol. 8.
- ⁶¹J. MacFarlane, I. Golovkin, P. Wang, P. Woodruff, and N. Pereyra, *High Energy Density Phys.* **3**, 181 (2007).
- ⁶²See <http://www.prism-cs.com/Software/Spect3D/overview.html> for “Prism Computational Sciences SPECT3D Overview.”
- ⁶³G. Moliere, *Z. Naturforsch. A* **3**, 78 (1948).
- ⁶⁴H. A. Bethe, *Phys. Rev.* **89**, 1256 (1953).
- ⁶⁵H. Bethe, *Ann. Phys.* **397**, 325 (1930).
- ⁶⁶E. Bonderup and P. Hvelplund, *Phys. Rev. A* **4**, 562 (1971).
- ⁶⁷C.-K. Li and R. D. Petrasso, *Phys. Rev. Lett.* **70**, 3059 (1993).
- ⁶⁸D. Gericke, *Laser Part. Beams* **20**, 471 (2002).
- ⁶⁹A. Zylstra, J. Frenje, P. Grabowski, C. Li, G. Collins, P. Fitzsimmons, S. Glenzer, F. Graziani, S. Hansen, S. Hu, M. G. Johnson, P. Keiter, H. Reynolds, J. Rygg, F. Séguin, and R. Petrasso, *Phys. Rev. Lett.* **114**, 215002 (2015).
- ⁷⁰A. B. Zylstra, C. K. Li, H. G. Rinderknecht, F. H. Séguin, R. D. Petrasso, C. Stoeckl, D. D. Meyerhofer, P. Nilson, T. C. Sangster, S. L. Pape, A. Mackinnon, and P. Patel, *Rev. Sci. Instrum.* **83**, 013511 (2012).
- ⁷¹A. A. Schekochihin, A. B. Iskakov, S. C. Cowley, J. C. McWilliams, M. R. E. Proctor, and T. A. Yousef, *New J. Phys.* **9**, 300 (2007).
- ⁷²P. Odier, J.-F. Pinton, and S. Fauve, *Phys. Rev. E* **58**, 7397 (1998).
- ⁷³P. Tzeferacos, A. Rigby, A. Bott, A. R. Bell, R. Bingham, A. Casner, F. Cattaneo, E. M. Churazov, J. Emig, N. Flocke, F. Fiuza, C. B. Forest, J. Foster, C. Graziani, J. Katz, M. Koenig, C.-K. Li, J. Meinecke, R. Petrasso, H.-S. Park, B. A. Remington, J. S. Ross, D. Ryu, D. Ryutov, K. Weide, T. G. White, B. Reville, F. Miniati, A. A. Schekochihin, D. H. Froula, G. Gregori, and D. Q. Lamb, *Phys. Plasmas* **24**, 041404 (2017).
- ⁷⁴R. L. Shepherd, D. R. Kania, and L. A. Jones, *Phys. Rev. Lett.* **61**, 1278 (1988).
- ⁷⁵P. Renaudin, C. Blancard, G. Faussurier, and P. Noiret, *Phys. Rev. Lett.* **88**, 215001 (2002).
- ⁷⁶A. P. L. Robinson, H. Schmitz, and P. McKenna, *New J. Phys.* **17**, 083045 (2015).